PHYSICAL REVIEW E **82**, 026307 (2010)

# Heat transfer and fluid flow in microchannels and nanochannels at high Knudsen number using thermal lattice-Boltzmann method

J. Ghazanfarian* and A. Abbassi†
*Mechanical Engineering Department, Amirkabir University of Technology, Tehran, Iran*

(Received 6 June 2010; published 13 August 2010)

The present paper deals with the two-dimensional numerical simulation of gaseous flow and heat transfer in planar microchannel and nanochannel with different wall temperatures in transitional regime $0.1 \leq \mathrm{Kn} \leq 1$. An atomistic molecular simulation method is used known as thermal lattice-Boltzmann method. The results of simulation are presented in four cases corresponding to the Fourier flow, shear-driven flow (Couette flow), pressure-driven flow (Poiseuille flow), and mixed shear–pressure-driven flow in the developing and fully developed regions. The mixed shear–pressure-driven flow is divided into two subcases with shear stress and pressure gradient acting in the same and the opposite directions. Normalized temperature and velocity profiles across the channel, distribution of local wall Nusselt number, and friction coefficient are illustrated. Using this method, nonlinear pressure distribution in the streamwise direction, reduction in mass flow rate, $C_f$ Re, and Nu by increasing the Knudsen number are studied. It is seen that for Couette flow, Nu over the hotter plate is greater than the cooler plate, but for the pressure-driven flow with stationary wall temperature dependency of viscosity and thermal conductivity causes this trend to be reversed. The reversed flow appearance in the velocity profile is captured in the case of opposite shear–pressure-driven flow.

DOI: 10.1103/PhysRevE.82.026307 PACS number(s): 47.55.pb, 47.11.−j, 44.05.+e, 47.61.−k

## I. INTRODUCTION

In last decades, many studies have been dedicated to the simulation of flow and heat transfer in microstructures and nanostructures. By decreasing the characteristic length of the problem from macroscale to nanoscale, the results of the classical continuum simulation of fluid flow and heat transfer start to deviate from experimental results. Therefore, atomistic methods such as lattice-Boltzmann method (LBM) have been frequently used to predict the gas behavior in the microscale to nanoscale geometries [1–4]. On the other hand, there are some attempts to simulate high Knudsen number heat transfer phenomenon using continuum laws such as conduction heat transfer [5]; up to $\mathrm{Kn}=10$, and Poiseuille flow [6]; and for the Knudsen numbers up to 0.4. But, still for nanoscale simulations of gaseous flow, atomistic methods are the only reliable methods [7].

Two-distribution function lattice-Boltzmann method (TDFLBM) is a strong tool to simulate nonisothermal gas flows in Micro Electro Mechanical Systems/Nano Electro Mechanical Systems (MEMS/NEMS). There are two categories of TDFLBMs. In the first category [8], two new variables are introduced for each distribution function to keep the consistency of the viscosity and to keep the scheme explicit. So, the lattice-Boltzmann equation is transformed to the new variables, while the boundary conditions are for the old variables. The second category of TDFLBMs proposed by Peng *et al.* [9] uses the same variable for both governing equations and boundary conditions which simplifies the calculation process and reduces the computational cost. This category does not include the complex gradient term in the evolution equations [9]. As a sample case of other atomistic methods, Hadjiconstantinou and Simek [7] employed the direct simulation Monte Carlo (DSMC) method to simulate pressure-driven flow and heat transfer in microchannels and nanochannels with constant wall temperatures in the slip and transitional regimes.

The lattice-Boltzmann equation (LBE) algorithm consists of collision and advection steps. For a given LBE model, the collision is the only step involving fixed arithmetic operations at each grid node, while the advection moves data from one grid node to another with no arithmetic operation. Obviously, for a system of size $N^3$, the overall computational cost of the LBE method is of $O(N^3)$ [10]. So, thermal lattice-Boltzmann method relative to the other atomistic methods has incredibly less computational cost [11].

The boundary condition is an important issue in the lattice-Boltzmann method. Many studies have been involved in the definition of proper boundary conditions of the thermal lattice-Boltzmann method for macroscale simulations [12–14] and microchannel to nanoscale simulations [15–18]. Ansumali and Karlin [15] derived the lattice-Boltzmann equation from the continuous kinetic theory in order to obtain boundary condition of diffusely reflecting moving solid wall. Thermal boundary condition for thermal lattice-Boltzmann equation was proposed by Niu *et al.* [16] by extending the diffuse scattering boundary condition (DSBC) to consider temperature jump at wall boundaries. A systematic description of the kinetic lattice-Boltzmann method, including the diffuse scattering boundary condition, definition of the relaxation time, and the regularization, was presented in [17]. Analytical calculation of slip flow in lattice-Boltzmann models with kinetic boundary conditions was presented by Sbragaglia and Succi [18]. They analytically and numerically showed that, in the presence of a nonzero slip coefficient, the lattice-Boltzmann flow develops a physical slip flow component at the wall. In this study it is shown that the slip coefficient can be tuned in such a way that one recovers quanti-

---

*j.ghazanfarian@aut.ac.ir
†abbassi@aut.ac.ir

tative agreement with analytical and experimental results up to the second order in the Knudsen number [18].

The extension of the standard lattice-Boltzmann methods to the higher-order velocities is studied in [19–21]. Shan *et al.* [19] presented in detail a theoretical framework for representing hydrodynamic systems through a systematic discretization of the Boltzmann kinetic equation. They showed that the conventional lattice-Boltzmann models can be directly derivable from this systematic approach. In addition, a clear and rigorous procedure for obtaining higher-order approximations to the continuum Boltzmann equation can be found in this work. A further theoretical extension to the kinetic-theory-based formulation of the lattice-Boltzmann method of Shan *et al.* is presented by Zhang *et al.* [20]. In this study they introduced the higher-order projection of the equilibrium distribution function, a sufficiently accurate Gauss-Hermite quadrature in the original formulation, and a regularization procedure. The velocity discretization is a critical step in deriving the lattice Boltzmann from the continuous Boltzmann equation. This problem is considered by Philippi *et al.* [21], following an alternative approach and giving the minimal discrete velocity sets in accordance with the order of approximation that is required for the LBE with respect to the continuous Boltzmann equation and with the lattice structure.

In this paper, the second category of TDFLBM is used to simulate flow and heat transfer in microchannel and nanochannel. In Sec. II, details of thermal lattice-Boltzmann method with definition of relaxation times are introduced. Modification of mean free path near solid walls and dependency of thermal conductivity and viscosity to the temperature and the density are presented in this section. Boundary conditions of two evolution equations with the simulated geometry are presented in Sec. III. Finally, the results of simulations for four different cases corresponding to the Fourier flow, shear-driven flow (Couette flow), pressure-driven flow (Poiseuille flow), and mixed shear–pressure-driven flow are discussed in Sec. IV. Section V concludes the paper.

## II. THERMAL LATTICE-BOLTZMANN METHOD

A simplified thermal lattice-Boltzmann model was proposed by Peng *et al.* [9] for incompressible thermal flows based on the work of He *et al.* [8]. They showed that the governing equations for density and internal energy distribution functions without heat dissipation and without external applied body force are

$$f_i(\mathbf{x}+\mathbf{e_i}\delta t, t+\delta t) - f_i(\mathbf{x},t) = -\frac{1}{\tau_v}[f_i(\mathbf{x},t) - f_i^{eq}(\mathbf{x},t)], \quad (1)$$

$$g_i(\mathbf{x}+\mathbf{e_i}\delta t, t+\delta t) - g_i(\mathbf{x},t) = -\frac{1}{\tau_c}[g_i(\mathbf{x},t) - g_i^{eq}(\mathbf{x},t)], \quad (2)$$

where $\tau_v$ and $\tau_c$ are nondimensional relaxation times, and $f_i(\mathbf{x},t)$ and $g_i(\mathbf{x},t)$ are density and internal energy distribution functions in position $\mathbf{x}$ and time $t$, respectively, which can be related by $g_i=[(\mathbf{c_i}-\mathbf{u})^2/2]f_i$. In these equations, "*eq*" superscript refers to the equilibrium density distribution functions [22] and can be computed from

$$f_i^{eq} = \rho\omega_i\left[1 + \frac{3\mathbf{c_i}\cdot\mathbf{u}}{c^2} + \frac{9\mathbf{c_i}\cdot\mathbf{u}^2}{2c^4} - \frac{3\mathbf{u}^2}{2c^2}\right], \quad (3)$$

in which particle velocity has been discretized as

$$\mathbf{c}_0 = (0,0),$$

$$\mathbf{c}_{i=1-4} = \left(\cos\left[\frac{(i-1)\pi}{2}\right], \sin\left[\frac{(i-1)\pi}{2}\right]\right)c,$$

$$\mathbf{c}_{i=5-8} = \sqrt{2}\left(\cos\left[\frac{(i-5)\pi}{2}+\frac{\pi}{4}\right], \sin\left[\frac{(i-5)\pi}{2}+\frac{\pi}{4}\right]\right)c. \quad (4)$$

Here, for the D2Q9 model, $c=\frac{\delta x}{\delta t}=\sqrt{3RT_0}=1$, where $T_0$ is the average temperature, $R$ is the universal gas constant, $\omega_0=\frac{4}{9}$, $\omega_{1,2,3,4}=\frac{1}{9}$, and $\omega_{5,6,7,8}=\frac{1}{36}$ [16]. The internal energy equilibrium distribution function depends on the density equilibrium distribution function through the temperature by [23]

$$g_i^{eq} = \epsilon f_i^{eq}. \quad (5)$$

The macroscopic properties of the gas can be computed from

$$\rho = \sum_i f_i, \quad \rho\mathbf{V} = \sum_i \mathbf{c_i} f_i, \quad \rho\epsilon = \sum_i g_i, \quad (6)$$

where $\epsilon=\frac{DRT}{2}$ is the internal energy and $D$ is the dimension of the problem ($D=2$). The kinematic viscosity ($\nu$) and thermal diffusivity ($\chi$) for a square lattice can be obtained from

$$\nu = \frac{1}{3}(\tau_v - 0.5)c^2\delta t, \quad \chi = \frac{2}{3}(\tau_c - 0.5)c^2\delta t. \quad (7)$$

The term −0.5 is a correction term to make the lattice-Boltzmann method a second-order scheme for incompressible flows [4]. For D2Q9 lattice BGK model, the Knudsen number can be obtained by

$$\mathrm{Kn} = \sqrt{\frac{8}{3\pi}}\frac{\tau_v - 0.5}{N_H}, \quad (8)$$

where $N_H$ is the number of lattice sites across the channel [4].

A wall function was proposed for the standard lattice BGK model which can accurately describe the nonlinear behavior of gas in the Knudsen layer for planar Couette heat transfer [24] and Poiseuille flow [3]. In the present study this wall function has been used for high Knudsen simulation of heat transfer for shear-driven, pressure-driven, and mixed shear–pressure-driven flows. Using this wall function for flow between parallel plates, the gas mean free path in the Knudsen layer can be modified as follows:

$$\lambda_e = \frac{\lambda}{1 + 0.7(e^{-Cy/\lambda} + e^{-C(H-y)/\lambda})}, \quad (9)$$

where $\lambda_e$ is the effective mean free path, and $y$ and $H-y$ are distances from the lower and the upper walls, respectively. $C$ is a constant which controls the growth of Knudsen layer and in this study was assumed to be 1.

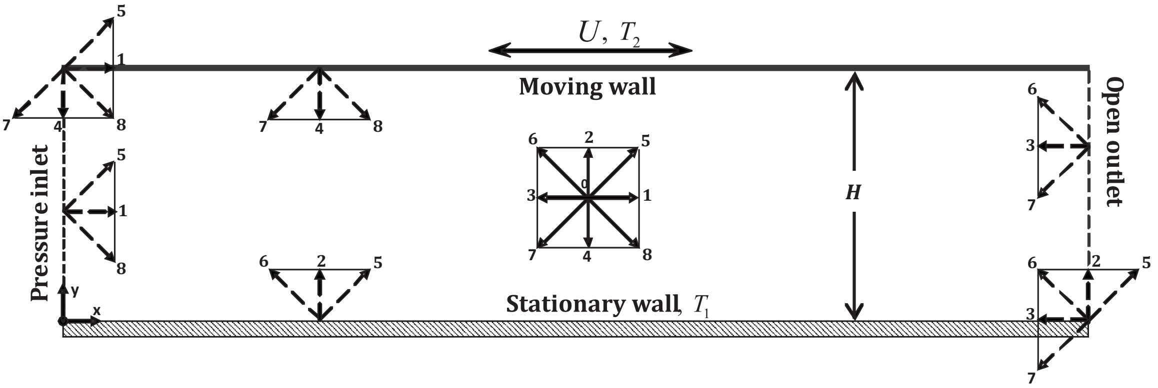

FIG. 1. Geometry and boundary conditions of the problem.

By decreasing the size of the geometry down to the microscales and nanoscales, the gas properties such as viscosity, thermal conductivity, and mean free path are no longer constants. The dependency of viscosity to the temperature variation can be modeled by $\rho\nu \propto T^{\omega}$, in which the value of $\omega$ depends on the molecular interaction model and by assuming Maxwellian interactions; its value is equal to 1 [3]. Finally, combining this model by Eq. (9), the modified value of $\tau_v$ can be written as follows:

$$\tau_v' = \frac{\tau_v - 0.5}{1 + \psi(y/\lambda) + \psi\left(\frac{H-y}{\lambda}\right)} \frac{\rho_{ref}}{\rho}\left(\frac{\epsilon}{\epsilon_{ref}}\right)^{\omega-0.5} + 0.5, \quad (10)$$

where $\epsilon_{ref}$ and $\rho_{ref}$ are internal energy and density at the reference temperature, and $\psi(x)=0.7e^{-Cx}$. Using this temperature-dependent relaxation time, LBE and Thermal Lattice-Bolyzmann Method (TLBM) are now coupled. The thermal relaxation time can be determined from

$$\tau_c = \frac{\tau_v - 0.5}{\mathrm{Pr}} + 0.5. \quad (11)$$

It is worth mentioning that a similar modification of relaxation time in order to include the dependency of viscosity on density has been reported in [1], which can be derived from Eq. (10) for $\omega=0.5$ and $\psi=0$. Therefore, using two-distribution function thermal lattice-Boltzmann equation (TLBE) allows us to simulate thermal flows with variable Pr number [8].

## III. BOUNDARY CONDITIONS

After finishing the collision step and then streaming the gas particles to the nearest neighbors, there are some density and internal energy distribution functions in special directions which have not been determined yet. For instance, as shown in Fig. 1, on the upper wall, there are no lattice sites above the wall to stream the information from to the directions 4, 7, and 8 of the specified upper wall node. At the corners, five undetermined distribution functions exist for each corner (for example 1, 4, 5, 7, and 8 for the upper left corner). Similar conditions with unknown incoming directions of the other boundaries and corners of the channel have been shown in Fig. 1. Consequently, in this section, the unknown distribution functions are computed based on the relations obtained from specified boundary conditions.

In order to model slip condition on the stationary and moving walls, fully DSBC has been used [15], which leads to

$$|(\mathbf{c_i} - \mathbf{u_w}) \cdot \mathbf{n}| f_i = \sum_{(\mathbf{c_{i'}} - \mathbf{u_w}) \cdot \mathbf{n} < 0} |(\mathbf{c_{i'}} - \mathbf{u_w}) \cdot \mathbf{n}| \times R_f(\mathbf{c_{i'}} \rightarrow \mathbf{c_i}) \mathbf{f_{i'}}, \quad (12)$$

where $\mathbf{i}$ and $\mathbf{i'}$ are the directions of reflected and incident particles, respectively; $\mathbf{n}$ is the inward unit normal vector, $\rho_w$ and $\mathbf{u_w}$ are density and velocity at the wall; and $R_f$ is the scattering kernel given by

$$R_f(\mathbf{c_{i'}} \rightarrow \mathbf{c_i}) = \frac{\mathbf{A_N}}{\rho_{\mathbf{w}}} [(\mathbf{c_i} - \mathbf{u_w}) \cdot \mathbf{n}] \mathbf{f_i^{eq}}|_{\mathbf{u=u_w}}. \quad (13)$$

For zero normal mass flow condition through the wall, the normalized coefficient $A_N$ can be obtained from

$$A_N = \rho_w \frac{\sum_i |(\mathbf{c_i} - \mathbf{u_w}) \cdot \mathbf{n}| f_i}{|(\mathbf{c_i} - \mathbf{u_w}) \cdot \mathbf{n}| f_i^{eq}|_{u=u_w} \sum_i |(\mathbf{c_{i'}} - \mathbf{u_w}) \cdot \mathbf{n}| f_{i'}}. \quad (14)$$

For D2Q9 model $A_N=6$. DSBC in LBM assumes that the gas particles reflected from the wall lose their precollision information and are redistributed in a way that mass flux through the wall is zero [16]. By assuming the Maxwellian diffuse reflection condition on the wall, the reflected molecules are in thermal equilibrium with the wall, so the unknown internal energy distribution functions can be computed from

$$g_i = \epsilon_w f_i, \quad (15)$$

where $\epsilon_w = DRT_w/2$ is the internal energy of the wall.

At the inlet of the channel, specified pressure (density) flow boundary condition has been applied according to the work of Zou and He [13]. Known density and zero vertical velocity component were assumed at the inlet and then $f_1$, $f_5$, $f_8$, and the horizontal velocity component have been calculated. For corner nodes at the inlet (upper one can be seen in Fig. 1), the similar procedure as explained by Zou and He [13] was applied. To apply fixed temperature at the inlet, i.e.,

TABLE I. Details of different cases considered in this study.

| Cases | $\frac{P_1}{P_2}$ | $U$ | Kn | Description |
|---|---|---|---|---|
| Case 1 | 1 | 0 | 0.158, 0.475, 1.58 | Fourier flow |
| Case 2 | 1 | $0.05c$ | 0.1, 0.2, 0.4, 0.6, 0.8, 1 | Developing Couette flow |
| Case 3 | 2 | 0 | 0.1, 0.2, 0.4, 0.6, 0.8, 1 | Developing Poiseuille flow |
| Case 4-A | $2, \frac{3}{2}$ | $0.05c$ | 0.1, 0.2, 0.4, 0.6, 0.8, 1 | Developing mixed flow: shear stress and pressure gradient in the same direction |
| Case 4-B | $\frac{2}{3}, \frac{1}{2}$ | $0.05c$ | 0.1, 0.2, 0.4, 0.6, 0.8, 1 | Developing mixed flow: shear stress and pressure gradient in the opposite directions |

$T_{in}$, the method introduced by D'Orazio *et al.* [26] was used to compute $g_1$, $g_5$, and $g_8$. In this method, the unknown distribution functions were supposed to be in equilibrium state with the following internal energy:

$$\epsilon^{eq} = \frac{6(\epsilon_{in} - \epsilon_p)}{1 + 3\frac{u_x}{c^2} + 3\frac{u_x^2}{c^4}}, \tag{16}$$

where $\epsilon_p$ is the sum of six known internal energy distribution functions at the inlet node after streaming step. The corner nodes of the inlet need especial treatment. After streaming $g_1$, $g_4$, $g_5$, $g_7$, and $g_8$ of the upper left corner can be determined by assumption of equilibrium state with the following internal energy:

$$\epsilon^{eq} = \frac{36(\epsilon_{in} - \epsilon_p)}{11 + 15\frac{u_x}{c^2} + 15\frac{u_x^2}{c^4}}. \tag{17}$$

Again in this equation, $\epsilon_p$ is the sum of four known internal energy distribution functions at the inlet corner node after streaming step. A similar procedure can be applied to the lower left corner node.

The unknown density distribution functions of the outlet nodes were computed by extrapolating from two neighboring interior lattice nodes [12]. For corner nodes located on the outlet (lower right corner, for instance), $f_2$, $f_5$, and $f_6$ were treated by DSBC, $f_7$ was extrapolated from interior nodes, and $f_3$ was calculated in a way that the specified outlet pressure is applied to the exit nodes using Eq. (6) and other computed distribution functions. All of the unknown internal energy distribution functions at the outlet containing corner nodes were computed by extrapolating from two neighboring interior lattice nodes.

The flow was assumed to be initially static with the constant inlet temperature all over the domain. Then, the equilibrium density and energy distribution functions computed by initial velocity and temperature were given to $f_i$ and $g_i$ as initial guesses. Going through the steady state, corresponding errors for velocity ($e_V$), pressure ($e_P$), and temperature ($e_\epsilon$), at time step $n$ were computed from

$$e_V = \frac{\sum_{i,j} \|\mathbf{V^n} - \mathbf{V^{n-1}}\|}{\sum_{i,j} \|\mathbf{V^n}\|}, \quad e_P = \frac{\sum_{i,j} |P^n - P^{n-1}|}{\sum_{i,j} P^n},$$

$$e_\epsilon = \frac{\sum_{i,j} |\epsilon^n - \epsilon^{n-1}|}{\sum_{i,j} \epsilon^n}, \tag{18}$$

where $n$ and $n-1$ represent the new and old time steps, respectively, and summations are over all lattice sites. The tolerance of residuals of pressure, velocity, and internal energy on convergence was set to $10^{-9}$.

## IV. NUMERICAL RESULTS

A two-dimensional channel flow between two parallel plates with different constant wall temperatures is considered. Details of different cases and corresponding Knudsen numbers studied in the paper have been listed in Table I. In Table I, $P_1$ and $P_2$ are the pressures at the inlet and the outlet of the channel, respectively, which for Couette and Fourier flows, the ratio of $P_1/P_2$ is 1 but for other two cases it is considered to be greater than unity. $U$ is the velocity of the upper plate which for Couette and mixed flows has nonzero values, but for Poiseuille and Fourier flows its value is zero. Case 4 is the combination of pressure- and shear-driven flows. In case 4-A, pressure gradient and shear stress amplify each other ($P_1 > P_2$ and $U > 0$), but in case 4-B they are in the opposite directions ($P_1 < P_2$ and $U > 0$).

For plane channel flow, local friction and heat transfer rate on each plate can be measured by the wall local friction coefficient $C_{f,x}$ and wall local Nusselt number $\mathrm{Nu}_x$. By defining Re based on $U_c$ which is the characteristic velocity of the problem and is equal to $U$ for cases 2, 4-A, and 4-B, and bulk velocity ($u_b$) for case 3, we have

$$C_{f,x}\,\mathrm{Re} = \frac{H}{\frac{1}{2}U_c}\frac{\partial u_x}{\partial n}\bigg|_w, \tag{19}$$

$$\mathrm{Nu}_x = -\frac{H}{\epsilon_{w,x} - \epsilon_{b,x}}\frac{\partial \epsilon_x}{\partial n}\bigg|_w, \tag{20}$$

where $n$ is the wall inward normal direction. The bulk temperature and velocity were defined as $\epsilon_{b,x} = \int_0^H \rho_x u_x \epsilon_x dy / \int_0^H \rho_x u_x dy$ and $u_{b,x} = \int_0^H \rho_x u_x dy / \int_0^H \rho_x dy$, respectively. Subscript $x$ shows the dependency on $x$ coordinate along the channel.

During simulations, for cases 3 and 4, the outlet density is fixed to 1 and the density at the inlet is varied according to

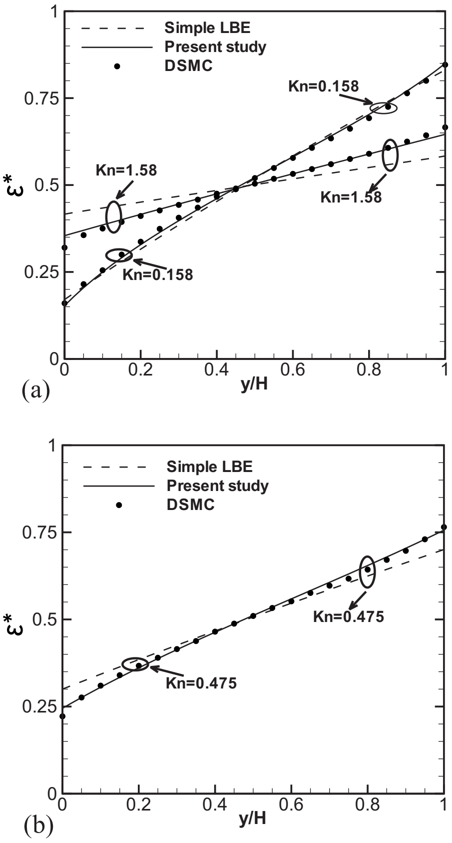

FIG. 2. Comparison of dimensionless internal energy profiles across the channel for Fourier flow: (a) Kn=0.156 and Kn=1.56; (b) Kn=0.475. Solid line, results of present study; dashed lines, results of present study without Knudsen layer modification; circles, DSMC results from [25].

Table I. For cases 2 and 4, the velocity of the moving plate is fixed at $U=0.05c$. Internal energies of the upper and the lower plates were supposed to be 1 and 2, respectively, and constant internal energy of 1.5 is imposed at the inlet. The reference internal energy and density are $\epsilon_{ref}=(\epsilon_1+\epsilon_2)/2$ and $\rho_{ref}=1$. A uniform grid of $801\times41$, corresponding to the aspect ratio $L/H=20$, is used for all mentioned cases which is long enough to allow the flow to be fully developed. The Prandtl number is fixed to 0.7 in all simulations. The velocity and internal energy will be shown in the following nondimensional forms:

$$u^*=\frac{u}{U_c},\qquad \epsilon^*=\frac{\epsilon-\epsilon_1}{\epsilon_2-\epsilon_1}. \tag{21}$$

Case 1, Fourier flow: This case has been used in order to verify the results of heat transfer simulations. So, in Fig. 2 for three Knudsen numbers from microscales to nanoscales, internal energy (temperature) profiles of the present study for Fourier flow are compared with DSMC results [25]. It is obvious that without Knudsen layer modification, temperature distribution near wall deviates from DSMC results. For small Knudsen numbers, the Knudsen layer correction is minimum, and by the increase in Kn the Knudsen layer corresponding to each plate will grow and eventually will overlap. This model is capable of capturing the nonlinear temperature distribution originating from Knudsen layer growth, for high Knudsen numbers with significantly less computational cost [3].

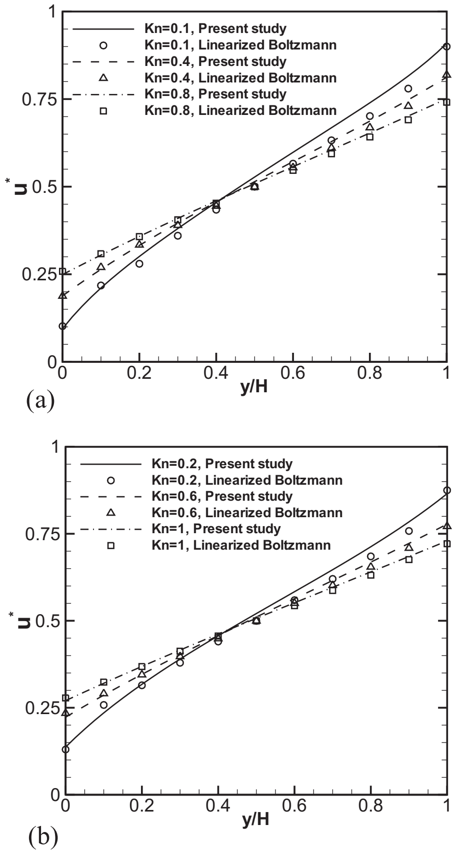

FIG. 3. Comparison of dimensionless velocity profiles across the channel for Couette flow: (a) Kn=0.1,0.4,0.8 and (b) Kn =0.2,0.6,1. Lines, results of present study; symbols, results of linearized Boltzmann equation from [27].

Case 2, Couette flow: The second case is a developing planar Couette flow with different wall temperatures with moving upper plate and stationary lower plate. Figure 3 was used to verify velocity filed simulation results of written numerical code by comparing nonisothermal velocity profiles corresponding to Kn=0.1–1, with velocity distributions obtained from the solution of linearized Boltzmann equation [27]. A slight deviation from the results of linearized Boltzmann equation stems from the temperature dependency of viscosity and thermal conductivity which cannot be considered in an isothermal solution. For Knudsen numbers 0.1 and 0.2, this deviation is expected to be greater due to the larger temperature difference between two plates, originating from smaller temperature jumps at the plate surfaces. It can be seen from Fig. 3 that values of $u^*|_{y/H=0.5}$ are not equal to 0.5 anymore due to the coupling of velocity and temperature fields. Again similar to case 1, Knudsen modification is necessary in order to capture nonlinear velocity and temperature profiles especially near solid walls.

Variations of total $C_f\,\mathrm{Re}$ and Nu separately for moving and stationary plates, with respect to Kn in the range of 0.1–1, are shown in Fig. 4. By increasing the Knudsen num-

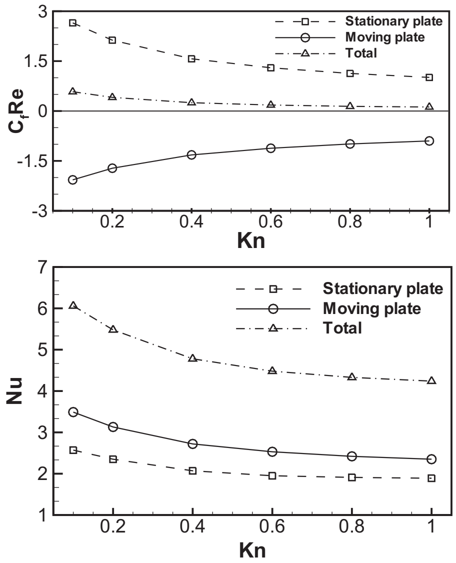

FIG. 4. Variation of $C_f$ Re and Nu for the upper plate, the lower plate, and total values versus the Knudsen number for Couette flow.

ber, both $C_f$ Re and Nu decrease due to the growth of rarefaction effects near walls. As is obvious from this figure, $C_f$ Re and Nu are not equal over moving and stationary plates. Approximately 40% larger Nu number for the upper plate relative to the lower plate originates from stronger thermal convection effects near upper plate due to the movement of the wall. In addition, another reason for different coefficients for two plates is the temperature dependency of viscosity and thermal conductivity which is a secondary reason in this case.

Case 3, Poiseuille flow: In this case, the upper plate is stationary and the specified pressures $P_1=2$ and $P_2=1$, corresponding to the strong pressure ratio of 2, are applied to the inlet and the outlet of the channel, respectively. Nonlinear pressure distribution has been considered in the simulations. Uniform internal energies (temperatures) of $\epsilon_{in}$, $\epsilon_1$, and $\epsilon_2$ are imposed at the inlet, the lower wall, and the upper wall, respectively. Also, temperature- and density-dependent viscosity and thermal conductivity with modification of mean free path near solid walls are used in the lattice-Boltzmann model of this study.

In Fig. 5, the nonisothermal fully developed normalized velocity profiles of present study across the channel for Kn $=0.1-1$ are compared with the solution of linearized Boltzmann equation presented by Ohwada *et al.* [28]. In the work of Ohwada *et al.* [28], the pressure gradient along the channel was small enough to ignore the compressibility effects. But in the present study, the pressure gradient in the streamwise direction is strong. So, the variation of viscosity and thermal conductivity with pressure (density) and temperature must be considered. As is obvious from Fig. 5, the results of the present study are in a good agreement with the results of linearized Boltzmann equation especially in the bulk flow regime. A slight deviation in the near wall flow regime is seen which stems from considering the compressibility effects, temperature-dependent viscosity in the flow simulations, and low-order velocity discretization (D2Q9). Tang *et al.* [2] ignored the compressibility effects by considering small pressure gradient along the channel for an isothermal solution. They showed that by using 13-velocity lattice model (D2Q13), velocity distribution near wall agrees well with the results of linearized Boltzmann equation.

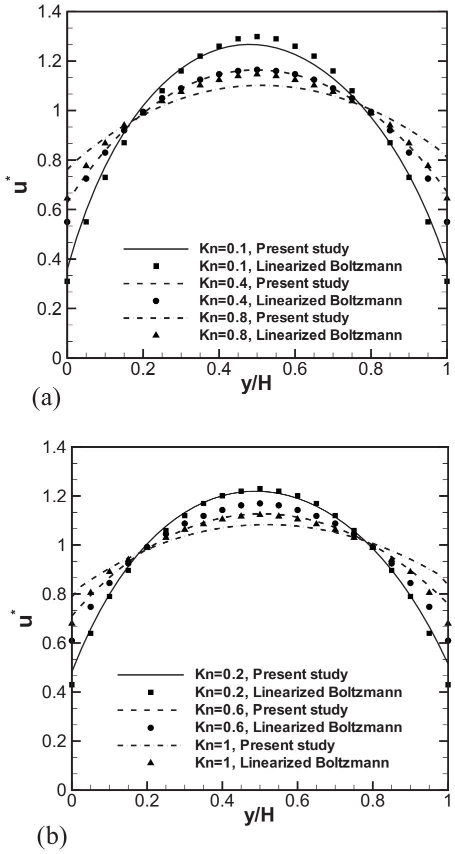

FIG. 5. Comparison of dimensionless velocity profiles across the channel for Poiseuille flow: (a) Kn=0.1, 0.4, 0.8 and (b) Kn $=0.2, 0.6, 1$. Lines, results of present study; symbols, results of linearized Boltzmann equation from [28].

Figure 5 shows an interesting point that, due to the variation of viscosity across the channel, the maximum value of velocity is shifted toward the cold plate (from $x/L=0.5$ to around $x/L=0.42$). This fact originates from the increasing of viscosity due to the increase in the temperature. Therefore, in the lower half of the channel the gas viscosity is smaller than in the upper half. So, the gas near cooler wall is accelerated and consequently the velocity in the lower half of the channel will be greater than the velocity on the other half.

Figure 6 presents normalized pressure deviation from linear pressure distribution along the channel, $(P-P_l)/P_2$, for different Knudsen numbers, where $P_l=P_2+(P_1-P_2)(1-x^*)$. This figure shows the compressibility effects in a nanochannel with strong pressure gradients. It is seen that by increasing the Knudsen number, $(P-P_l)/P_2$ becomes negative. Similar behavior have been reported previously by Nie *et al.* [1] for isothermal study of fluid flow in a nanochannel.

Internal energy (temperature) profiles of planar Poiseuille flow corresponding to the microscale to nanoscale (Kn $=0.1-1$) are illustrated in Fig. 7. As explained in Eq. (10), both thermal conductivity and viscosity strongly depend on

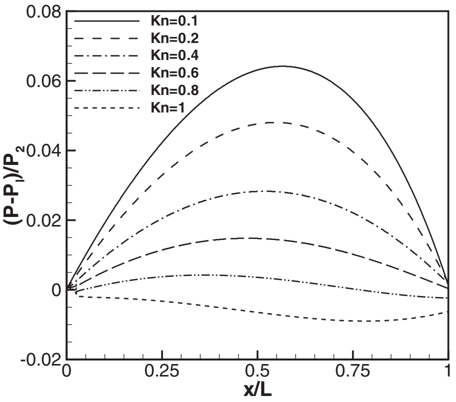

FIG. 6. Deviations from the linear pressure distribution in the streamwise direction for various Kn numbers.

density and temperature, which makes the temperature profile deviate from linear distribution. By increasing the Knudsen number, the curvatures of temperature profile near two solid walls propagate into the flow bulk, which shows the growth of the Knudsen layer near walls. Approximately after Kn=0.5, two Knudsen layers are combined and the curvature of temperature profile is disappeared.

For developing microchannel and nanochannel flows, friction factor and heat transfer rate corresponding to $C_f$ and Nu, respectively, are the most interesting parameters. Again in this case, Fig. 8 clearly shows that both $C_f$ Re and Nu have different values for the upper and lower plates. This fact only originates from the temperature dependency of viscosity and thermal conductivity since plates are stationary. Regardless of case 2, it is interesting that in this case Nu on the lower plate is approximately 10% greater than Nu on the upper plate. The reason for this fact can be recognized by referring to Eqs. (10) and (11), from which the thermal conductivity coefficient near hotter upper plate is greater than that near cooler lower plate. So, the Nusselt number $(\mathrm{Nu}=\frac{hH}{k})$ of the cooler plate is larger than that of the hotter plate.

Case 4, mixed flow: In this case, the combination of two previous cases 2 and 3, corresponding to the developing Couette flow and developing Poiseuille flow, respectively, has been simulated. As listed in Table. I, in case 4-A pressure gradient and shear stress act in a same direction which amplify each other. But, in case 4-B, the outlet pressure is considered to be greater than the inlet pressure which means that the pressure gradient and shear stress are acting in the opposite directions.

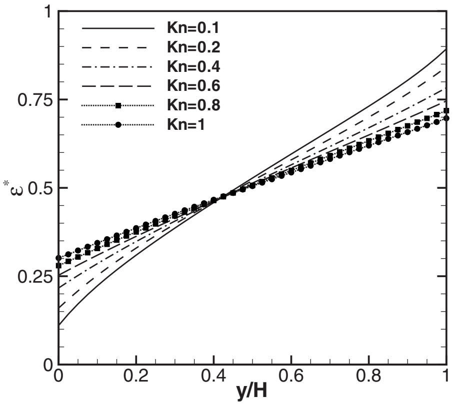

FIG. 7. Variation of dimensionless internal energy for Poiseuille flow across the channel and different Knudsen numbers.

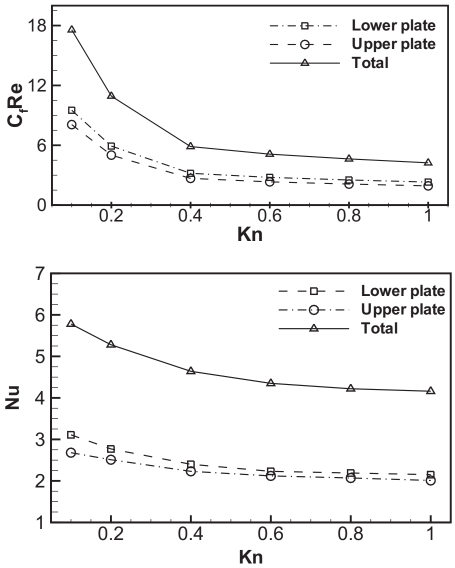

FIG. 8. Variation of $C_f$ Re and Nu for the upper plate, the lower plate, and total values versus the Knudsen number for Poiseuille flow.

Figure 9 illustrates the normalized velocity profiles across

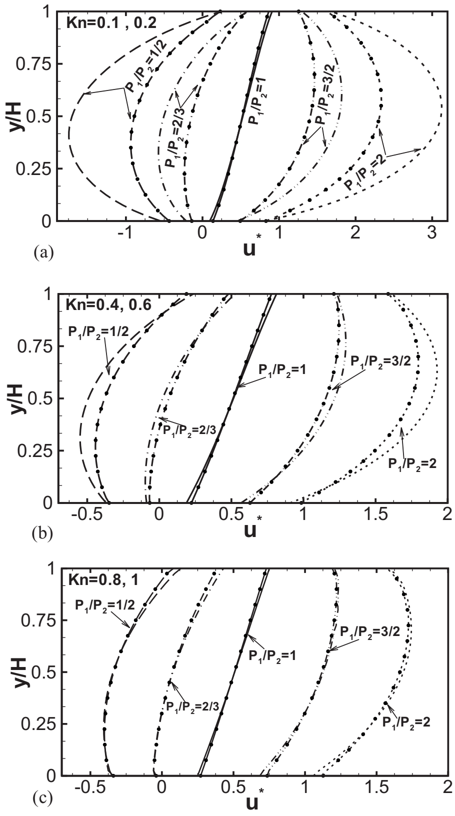

FIG. 9. Mixed flow velocity profiles across the channel for five different values of pressure gradients and $U=0.05$. Simple lines, Kn=0.1, 0.4, 0.8; lines with circles, Kn=0.2, 0.6, 1.

the channel for Kn=0.1–1 and five different pressure ratios. The velocity is normalized with the velocity of moving plate. In this figure, $P_1/P_2=1$, $P_1/P_2=2,3/2$, and $P_1/P_2=1/2,2/3$ demonstrate cases 2, 4-A, and 4-B, respectively. As is expected, by increasing the Knudsen number, the velocity slip on the moving and the stationary plates increases. This fact leads to the reduction in mass flow rate of the gas through the channel by increasing rarefaction effect.

By decreasing the pressure ratio and finally reversing its direction in case 4-B, the backflow with negative velocity magnitudes in the lower half of the channel gradually appears. The reversed flow makes the mass flow rate decrease and finally become negative. For the pressure ratio of $P_1/P_2=2/3$ in Fig. 9, by increasing the Knudsen number from 0.1 to 1, the nondimensional position of zero velocity across the channel moves approximately from $x/H=0.81$ to 0.31. This trend means that by increasing the Knudsen number, the area of reversed flow region shrinks. Consequently, by increasing the Knudsen number, the negative mass flow rate will increase or the absolute value of mass flow rate will decrease.

## V. CONCLUSION

In conclusion, the simulation results of thermal lattice-Boltzmann method in the present study shows that this method is capable of modeling shear-driven, pressure-driven, and mixed shear–pressure-driven rarified flows and heat transfer up to Kn=1 in the transitional regime. The compressibility effects are considered by imposing strong pressure gradient to the channel ports in mixed and pressure-driven cases. The effect of dependency of thermal conductivity and viscosity on the temperature and the density is studied and local Nu and $C_f$ Re over cooler and hotter plates are calculated for different Knudsen numbers up to 1. It is seen that for Couette flow, Nu over the hotter plate is greater than the cooler plate due to the convection effects near moving wall, but for the pressure-driven flow with stationary walls temperature dependency of viscosity and thermal conductivity causes this trend to be reversed. The reversed flow appearance in the velocity profile is captured in the case of opposite shear–pressure-driven flow, and the influence of rarefaction on the increase in slip velocity and decrease in mass flow rate is discussed.

[1] X. Nie, G. D. Doolen, and S. Chen, J. Stat. Phys. **107**, 279 (2002).

[2] G. H. Tang, Y. H. Zhang, X. J. Gu, and D. R. Emerson, EPL **83**, 40008 (2008).

[3] Y. H. Zhang, X. J. Gu, R. W. Barber, and D. R. Emerson, EPL **77**, 30003 (2007).

[4] Y. H. Zhang, R. S. Qin, Y. H. Sun, R. W. Barber, and D. R. Emerson, J. Stat. Phys. **121**, 257 (2005).

[5] J. Ghazanfarian and A. Abbassi, Int. J. Heat Mass Transfer **52**, 3706 (2009).

[6] F. Bao and J. Lin, Int. J. Heat Mass Transfer **51**, 4139 (2008).

[7] N. G. Hadjiconstantinou and O. Simek, J. Heat Transfer **124**, 356 (2002).

[8] X. He, S. Chen, and G. D. Doolen, J. Comput. Phys. **146**, 282 (1998).

[9] Y. Peng, C. Shu, and Y. T. Chew, Phys. Rev. E **68**, 026701 (2003).

[10] Y. Peng, W. Liao, L. S. Luo, and L. P. Wang, Comput. Fluids **39**, 568 (2010).

[11] G. H. Tang, X. J. Gu, R. W. Barber, D. R. Emerson, and Y. H. Zhang, Phys. Rev. E **78**, 026706 (2008).

[12] S. Chen, D. Martinez, and R. Mei, Phys. Fluids **8**, 2527 (1996).

[13] Q. Zou and X. He, Phys. Fluids **9**, 1591 (1997).

[14] G. H. Tang, W. Q. Tao, and Y. L. He, Phys. Rev. E **72**, 016703 (2005).

[15] S. Ansumali and I. V. Karlin, Phys. Rev. E **66**, 026311 (2002).

[16] X. D. Niu, C. Shu, and Y. T. Chew, Comput. Fluids **36**, 273 (2007).

[17] X. D. Niu, S. A. Hyodo, T. Munekata, and K. Suga, Phys. Rev. E **76**, 036711 (2007).

[18] M. Sbragaglia and S. Succi, Phys. Fluids **17**, 093602 (2005).

[19] X. Shan, X. F. Yuan, and H. Chen, J. Fluid Mech. **550**, 413 (2006).

[20] R. Zhang, X. Shan, and H. Chen, Phys. Rev. E **74**, 046703 (2006).

[21] P. C. Philippi, L. A. Hegele, Jr., L. O. E. dos Santos, and R. Surmas, Phys. Rev. E **73**, 056702 (2006).

[22] Y. Qian, D. d'Humieres, and P. Lallemand, EPL **17**, 479 (1992).

[23] Y. Shi, T. S. Zhao, and Z. L. Guo, Phys. Rev. E **70**, 066310 (2004).

[24] G. H. Tang, Y. H. Zhang, and D. R. Emerson, Phys. Rev. E **77**, 046701 (2008).

[25] M. A. Gallis, D. J. Rader, and J. R. Torczynski, Phys. Fluids **14**, 4290 (2002).

[26] A. D'Orazio, M. Corcione, and G. P. Celata, Int. J. Therm. Sci. **43**, 575 (2004).

[27] Y. Sone, S. Takata, and T. Ohwada, Eur. J. Mech., B/Fluids **9**, 273 (1990).

[28] T. Ohwada, Y. Sone, and K. Aoki, Phys. Fluids A **1**, 2042 (1989).